AIAA JOURNAL
Vol. 42, No. 5, May 2004

Reynolds Number Effects on Three-Dimensional Vorticity in a Turbulent Wake

M. W. Yiu* and Y. Zhou†
Hong Kong Polytechnic University, Hong Kong, People's Republic of China
T. Zhou‡
Nanyang Technological University, Singapore 639798, Republic of Singapore
and
L. Cheng§
Hong Kong Polytechnic University, Hong Kong, People's Republic of China

When Reynolds number Re ($\equiv U_\infty d/\nu$, where U_∞ is the free stream velocity, d is the cylinder diameter, and ν is the kinematic viscosity of fluid) varies from 10^3 to 10^4, there is a large change in the turbulent near-wake dynamics (e.g., the base pressure coefficient, fluctuating lift coefficient, and vortex formation length) of a circular cylinder, which has previously been connected to the generation of small-scale Kelvin–Helmholtz vortices. This work aims to investigate how this Re variation affects the three components of the vorticity vector and to provide a relatively complete set of three-dimensional vorticity data. All three components of vorticity were simultaneously measured in the intermediate region of a turbulent circular-cylinder wake using a multiwire vorticity probe. It is observed that the root-mean-square values of the three vorticity components increase with Re, especially the streamwise component, which shows a large jump from $Re = 5 \times 10^3$ to $Re = 10^4$. At $Re = 2.5 \times 10^3$, the maximum phase-averaged spanwise vorticity variance $\langle\omega_z^2\rangle^*$, normalized by d and U_∞, is twice as large as its counterpart for the streamwise component, $\langle\omega_x^2\rangle^*$, or the lateral component, $\langle\omega_y^2\rangle^*$. However, at $Re = 10^4$, the maximum $\langle\omega_z^2\rangle^*$ is only 55% larger than the maximum $\langle\omega_x^2\rangle^*$ or 47% larger than the maximum $\langle\omega_y^2\rangle^*$. The observation is consistent with the perception that the three-dimensionality of the flow is enhanced at higher Re due to the occurrence of Kelvin–Helmholtz vortices. The effect of Re on vorticity signals, spectra, and coherent and incoherent vorticity fields is also examined.

I. Introduction

FLOW around a circular cylinder has been a subject of intensive interest to engineers and scientists for many decades. The Reynolds number, Re ($\equiv U_\infty d/\nu$, where U_∞ is the free stream velocity, d is the cylinder diameter, and ν is the kinematic viscosity of fluid), has a profound effect on the near-wake dynamics. This effect has attracted a great deal of attention in the literature, particularly in the range of $Re = 10^3$–10^4. In this range, the Strouhal number Sr and the drag coefficient C_D experience mild variation.[1] However, there is a large change in the formation length of Kármán vortices,[2] and the mean base pressure coefficient $-C_{\mathrm{pb}}$ exhibits an almost 50% increase.[3] The fluctuating lift coefficient C_L' displays a drastic increase from nearly zero at $Re = 1.0 \times 10^3$ to about 0.4 at $Re = 1.0 \times 10^4$ (Refs. 1 and 4–6). Accordingly, the velocity fluctuation in the shear layer around the cylinder increases significantly.[4,7] Instantaneous structures show the generation of small-scale Kelvin–Helmholtz vortices, particularly evident at $Re = 5 \times 10^3$ and even more so at $Re = 1.0 \times 10^4$ (Ref. 8). One interesting question to be asked is how these near-wake variations with Re would impact upon the downstream wake. This work aims to investigate the Re effect on the evolution of the three-dimensional vorticity, which is an important characteristic of turbulence, in the intermediate wake.

There have been very limited experimental data on vorticity in a turbulent near or intermediate wake. The measurement of vorticity has proven to be a challenge,[9–11] especially when all three components of the vorticity vector are needed. Marasli et al.[9] presented the root-mean-square (rms) values of the three simultaneously measured vorticity components only at $x/d = 30$ and $Re = 2.0 \times 10^3$. Mi and Antonia[12] obtained the spanwise and lateral vorticity components separately using a probe consisting of two X wires for $x/d = 10$–70 at $Re = 3.0 \times 10^3$, without measuring the streamwise component. Zhang et al.'s[13] measurement of the three vorticity components covered $x/d = 20$ to 40 at $Re = 5.6 \times 10^3$ but suffered from poor spatial resolution. Therefore, another objective of the present work is to provide reliable three-dimensional vorticity data over $x/d = 10$ to 40 from both coherent and incoherent vorticity fields. These data are important for the thorough understanding of turbulent flow and the validation of turbulence models.

A vorticity probe in general consists of multiple hot wires. The first attempt to measure all three components of the vorticity vector was made by Wassman and Wallace[14] using a nine-wire probe. To avoid cross-talk between the wires, this probe was later refined and tested by Balint et al.,[15] Vukoslavcevic and Wallace,[16] and Tsinober et al.[17] and was used by Marasli et al.[9] to measure simultaneously the three components of vorticity in a turbulent intermediate wake. Using a simpler configuration, Zhu and Antonia[18] employed four X wires, with two aligned in the x–y plane (see Figs. 1a and 1b for sketches of the probe) and the others in the y–z plane, to measure all three components of the vorticity vector in a turbulent far wake. Attractive features of the probe include its ease of construction, the use of a standard yaw–pitch calibration for an X wire, and the potential for spatial resolution to be corrected.

Experimental details and data processing are described in Sec. II. Section III presents the instantaneous signals, probability density functions, and rms values of the three components of the vorticity vector, followed by the coherent vorticity fields (Sec. IV) and contributions from the coherent structures to three vorticity components (Sec. V). The work is concluded in Sec. VI.

Received 3 March 2003; revision received 18 December 2003; accepted for publication 18 December 2003.

*Research Student, Department of Mechanical Engineering, Hung Hom, Kowloon.
†Associate Professor, Department of Mechanical Engineering, Hung Hom, Kowloon; mmyzhou@polyu.edu.hk.
‡Assistant Professor, School of Mechanical and Production Engineering.
§Professor, Department of Mechanical Engineering, Hung Hom, Kowloon.

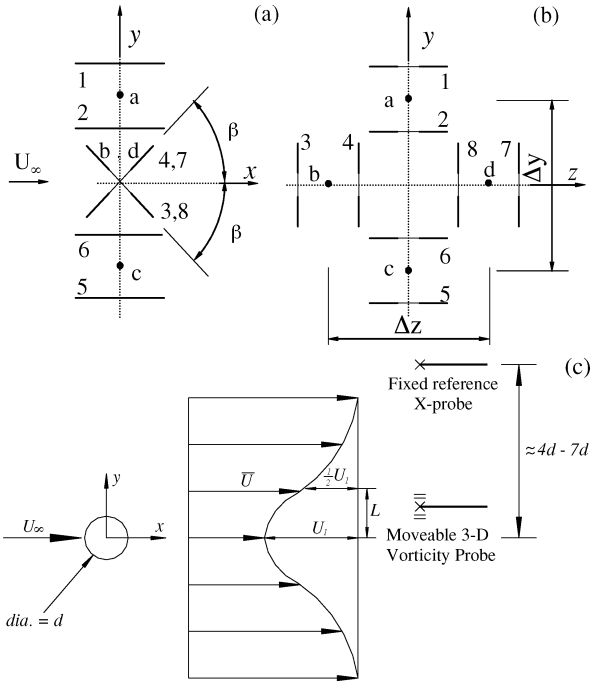

Fig. 1 Sketches of the vorticity probe and experimental arrangement: a) side view of the probe, b) front view of the probe, and c) experimental arrangement.

II. Experimental Details

Measurements were conducted in an open-return low-turbulence wind tunnel at the University of Newcastle with a working section of 0.35 m × 0.35 m and 2.4 m long. A circular cylinder with diameter $d = 12.7$ mm was used to generate the wake. The free stream velocity U_∞ were 3, 6, and 12 m/s, resulting in $Re = 2.5 \times 10^3$, 5.0×10^3, and 1.0×10^4. A probe consisting of four X wires (Figs. 1a and 1b) was used to measure all three components of the vorticity vector simultaneously. Two of the X wires were aligned in the x–y plane and separated by $\Delta z = 1.9$ mm in the z direction; the other two were in the x–z plane and separated by $\Delta y \approx \Delta z$ in the y direction. These separations correspond here to $\Delta z \approx \Delta y \approx 8 - 30\eta$, where $\eta \equiv (\nu^3/\langle\varepsilon\rangle)^{1/4}$ is the Kolmogorov length scale and $\langle\varepsilon\rangle$ is the mean energy dissipation rate. By using the present probe, 9 of the 12 velocity derivative correlations involved in the expression for $\langle\varepsilon\rangle$ can be measured simultaneously. The quantities $\langle(\partial v/\partial y)^2\rangle$ and $\langle(\partial w/\partial z)^2\rangle$ cannot be measured directly. However, they can be obtained indirectly from continuity, viz.,

$$\frac{\partial u}{\partial x} + \frac{\partial v}{\partial y} + \frac{\partial w}{\partial z} = 0 \tag{1a}$$

or

$$2\left\langle\left(\frac{\partial v}{\partial y}\right)^2\right\rangle + 2\left\langle\left(\frac{\partial w}{\partial z}\right)^2\right\rangle = 2\left\langle\left(\frac{\partial u}{\partial x}\right)^2\right\rangle - 4\left\langle\left(\frac{\partial v}{\partial y}\right)\left(\frac{\partial w}{\partial z}\right)\right\rangle \tag{1b}$$

By assuming homogeneity, the last term in Eq. (1b) can be replaced by $4\langle(\partial v/\partial z)(\partial w/\partial y)\rangle$ and the mean energy dissipation rate can be expressed as

$$\begin{aligned}\langle\varepsilon\rangle = \nu\Bigg\{&4\left\langle\left(\frac{\partial u}{\partial x}\right)^2\right\rangle + \left\langle\left(\frac{\partial u}{\partial y}\right)^2\right\rangle + \left\langle\left(\frac{\partial v}{\partial x}\right)^2\right\rangle + \left\langle\left(\frac{\partial u}{\partial z}\right)^2\right\rangle \\ &+ \left\langle\left(\frac{\partial w}{\partial x}\right)^2\right\rangle + \left\langle\left(\frac{\partial v}{\partial z}\right)^2\right\rangle + \left\langle\left(\frac{\partial w}{\partial y}\right)^2\right\rangle + 2\left\langle\left(\frac{\partial u}{\partial y}\right)\right\rangle\left\langle\left(\frac{\partial v}{\partial x}\right)\right\rangle \\ &+ 2\left\langle\left(\frac{\partial u}{\partial z}\right)\right\rangle\left\langle\left(\frac{\partial w}{\partial x}\right)\right\rangle - 2\left\langle\left(\frac{\partial v}{\partial z}\right)\right\rangle\left\langle\left(\frac{\partial w}{\partial y}\right)\right\rangle\Bigg\}\end{aligned} \tag{1c}$$

Table 1 Kolmogorov length scales (millimeters) at various locations and Reynolds numbers

x/d	$Re = 2.5 \times 10^3$	$Re = 5.0 \times 10^3$	$Re = 1.0 \times 10^4$
10	0.17	0.12	0.076
20	0.22	0.14	0.09
40	0.31	0.2	0.12

All of these terms can be measured by the present probe. The values of $\langle\varepsilon\rangle$ obtained from Eq. (1c) are used to calculate the Kolmogorov length scale η. These values are given in Table 1. The separation between the two inclined wires of each X wire was about 0.6 mm. Another X wire, placed at $y = 4$–$7d$, depending on the measurement station $x/d = 10$–40, was used in conjunction with the vorticity probe in order to provide a phase reference for the measured vorticity signals (Fig. 1c).

The hot wires were etched from Wollaston (Pt–10% Rh) wires. The active length was about $200d_w$, where $d_w = 2.5$ μm is the wire diameter. The wires were operated on in-house constant-temperature circuits at an overheat ratio of 0.5. The probe was calibrated at the centerline of the tunnel using a pitot static tube connected to a MKS Baratron pressure transducer (least count = 0.01 mm H_2O). The yaw calibration was performed over ±20 deg. The included angle of each X wire was about 110 deg and the effective angle of the inclined wires was about 35 deg, which was sufficient to minimize the effect of large velocity cone angles (e.g., Perry et al.[19] and Browne et al.[20]). Output signals from the anemometers were passed through buck and gain circuits and low-pass filtered at a cutoff frequency f_c close to $\bar{U}/2\pi\eta$, which is commonly identified as the Kolmogorov frequency f_K, where $\bar{U}$ is the local mean velocity in the streamwise direction. The filtered signals were subsequently sampled at a frequency $f_s = 2f_c$ using a 12-bit analog-to-digital converter. The duration of data was about 60 s.

It is assumed that each X probe measures the two velocity components at the center of the probe. While measured velocity components can be significantly in error when the velocity gradients are large,[16,21,22] the mean velocity gradient is not significant in the present flow. Using a range of hot-wire yaw factors corresponding to these experimental conditions, errors in neglecting the fluctuating instantaneous velocity gradients are estimated to be about 3% and 4% for $u_{\rm rms}$ and $v_{\rm rms}$ (or $w_{\rm rms}$), respectively, where u, v, and w are the velocity fluctuations in the x, y, and z directions, respectively. The binormal cooling effect on each X probe has also been neglected, which only gives rise to an error of 1–3% for $u_{\rm rms}$ and $v_{\rm rms}$ (or $w_{\rm rms}$) when the local turbulence intensity is about 10%.[23] The present $u_{\rm rms}/\bar{U}$ ranges from 20% to 10% for $x/d = 10$–40. Therefore, the error in neglecting the binormal cooling effect is estimated to be about 4%. Experimental uncertainties in $\bar{U}$ and $u_{\rm rms}$ (or $v_{\rm rms}$ and $w_{\rm rms}$) were inferred from errors in the hot-wire calibration data as well as the scatter (20 to 1 odds) observed in repeating the experiment a number of times. The uncertainty for $\bar{U}$ was about ±2%, while uncertainties for $u_{\rm rms}$, $v_{\rm rms}$, and $w_{\rm rms}$ were about ±5%, ±6%, and ±6%, respectively.

The vorticity components are calculated from the measured velocity signals, viz.,

$$\omega_x = \frac{\partial w}{\partial y} - \frac{\partial v}{\partial z} \approx \frac{\Delta w}{\Delta y} - \frac{\Delta v}{\Delta z} \tag{2}$$

$$\omega_y = \frac{\partial u}{\partial z} - \frac{\partial w}{\partial x} \approx \frac{\Delta u}{\Delta z} - \frac{\Delta w}{\Delta x} \tag{3}$$

$$\omega_z = \frac{\partial v}{\partial x} - \frac{\partial(\bar{U}+u)}{\partial y} = \frac{\Delta v}{\Delta x} - \frac{\Delta(\bar{U}+u)}{\Delta y} \tag{4}$$

where Δw and Δu in Eqs. (2) and (4) are velocity differences between X wires a and c (Figs. 1a and 1b); Δv and Δu in Eqs. (2) and (3) are velocity differences between X wires b and d. The spatial separation Δx is estimated based on Taylor's hypothesis, given by $-U_c(2\Delta t)$, where U_c is the average convection velocity of vortices, given by $0.87 \sim 0.89U_\infty$, depending on the streamwise location,[24]

and $\Delta t \equiv 1/f_s$ is the time interval between two consecutive points in the time series of velocity signals. This method would have the advantages of allowing $\Delta x \approx \Delta y \approx \Delta z$, to avoid phase shift[10] and to maintain the same level of spectral attenuation for the same Reynolds number between the velocity gradients occurring in Eqs. (2–4). Because of limited spatial resolution of the probe, the velocity derivatives in the vorticity components are expected to be underestimated. The errors in measuring vorticity components at $x/d = 10$, 20, and 40 are estimated to be about 28%, 18%, and 10% for $Re = 2.5 \times 10^3$, 41%, 33%, and 22% for $Re = 5.0 \times 10^3$, and 68%, 55%, and 41% for $Re = 1.0 \times 10^4$, respectively.

III. Characteristics of the Three Vorticity Components

A. Vorticity Signals

Vorticity is derived from velocity fluctuations measured by the four X wires. Measured velocity signals may be erroneous if the probe is not constructed properly, especially because of inappropriate effective angles. To examine the appropriateness of effective angles, the probability density functions (pdfs) of the velocity vector angle (β) at $x/d = 10$ for different Reynolds numbers are calculated and shown in Fig. 2. The velocity vector angle is calculated based on the instantaneous longitudinal and transverse velocity components, U and V. For all Reynolds numbers, the velocity vector angles are comparable. The probability that the velocity vector angles exceed ± 35 deg is only 0.1%, resulting in a negligible effect on measured velocity fluctuations. Note that β may be larger than the calibration yaw angle (± 20 deg). Ideally, the yaw angle should exceed the largest β. However, Browne et al.[25] found that the dependence of the effective angle of the X wire on the yaw angle was negligible over the range from -40 to 15 deg and concluded that the calibration yaw angle range of ± 15 deg was adequate for flows with a moderate turbulence intensity. Furthermore, for all Re investigated, only 8% of β for $y/d \leq 1.0$ are larger than the maximum yaw angle (± 20 deg). The percentage drops to 2% for a larger y/d. It is therefore concluded that the errors due to a relatively small range of yaw angles for calibration may be negligible.

Figure 3 presents the instantaneous signals of ω_x, ω_y, and ω_z, along with that of v, near the most likely vortex location ($y/d = 0.6$) (Refs. 26 and 27) at $x/d = 10$ for $Re = 2.5 \times 10^3$, 5.0×10^3, and 1.0×10^4, where an asterisk denotes normalization by d and U_∞. (The arrow indicates the direction of the flow. The dots and dashed vertical lines on the v signals indicate possible vortex centers. The horizontal lines are zero levels of the signals.) The v- and ω_z-signals for all Re display large-scale quasi-periodical fluctuations, indicating the occurrence of Kármán vortices. The zero v of positive dv/dt generally corresponds to the large-scale ω_z fluctuations of negative sign and is identified with the possible Kármán vortex center, marked by a dot in the v-signal. The fluctuations, near the vortex centers, of the ω_x- and ω_y-signals conform to the three-dimensionality of Kármán vortices. The ω_x- and ω_y-signals display significant fluctuations in either sign between spanwise vortex centers, which could be linked to the occurrence of quasi-longitudinal rib structures.[13,26,28] As Re increases, small-scale fluctuations in the vorticity signals increase, particularly evident as Re changes from 5.0×10^3 to 1.0×10^4. The observation is consistent with the previous report,[8] based on high-image-density particle-image velocimetry, that small-scale Kelvin–Helmholtz vortices were evident at $Re = 5.0 \times 10^3$ and more so at $Re = 1.0 \times 10^4$. It could be inferred that the Kelvin–Helmholtz vortices are partially responsible for the increased three-dimensionality of the flow.

B. Probability Density Function

Figure 4 shows the pdfs, $P(\omega_x)$, $P(\omega_y)$ and $P(\omega_z)$, calculated based on vorticity signals measured near the most probable vortex path ($y/d = 0.6$) at $x/d = 10$. The abscissa has been normalized by the root-mean-square vorticity. $P(\omega_x)$ (Fig. 4a) is quite symmetric about zero for $Re = 2.5 \times 10^3$ and 5.0×10^3 but shows a slightly skewed peak for $Re = 1.0 \times 10^4$. This skewness is probably

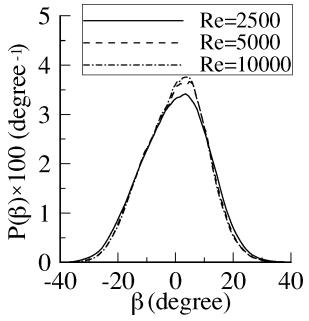

Fig. 2 PDF of velocity vector angles, $\beta = \tan^{-1}(V/U)$, at $x/d = 10$.

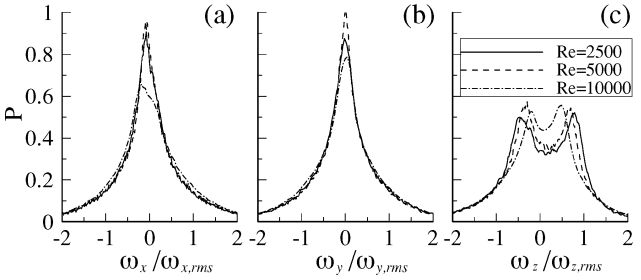

Fig. 4 Probability density function of vorticity at $y/d = 0.6$ and $x/d = 10$: a) $P(\omega_x)$, b) $P(\omega_y)$, and c) $P(\omega_z)$.

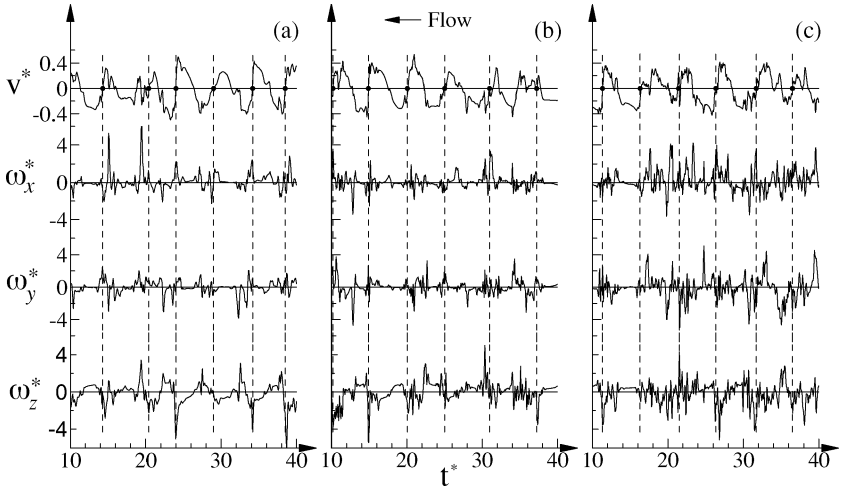

Fig. 3 Instantaneous signals of transverse velocity and three vorticity components on the vortex center ($y/d = 0.6$) at $x/d = 10$: a) $Re = 2.5 \times 10^3$, b) $Re = 5.0 \times 10^3$, and c) $Re = 1.0 \times 10^4$.

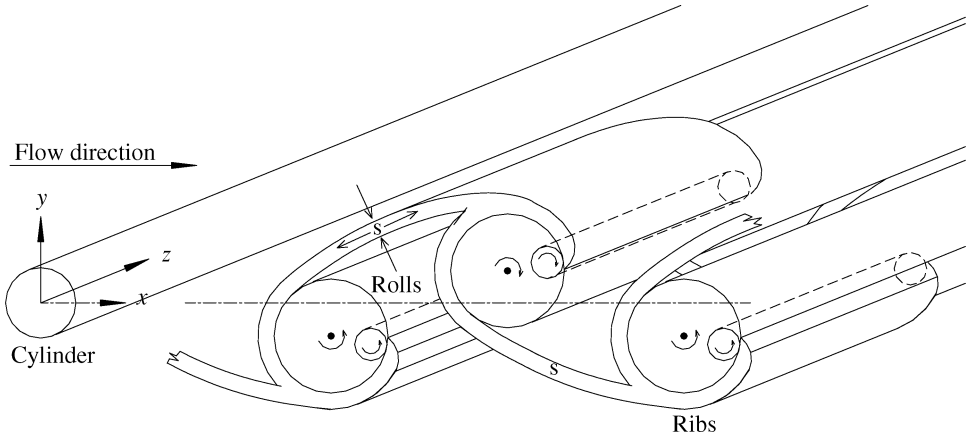

Fig. 5 Three-dimensional conceptual spatial relationship between the spanwise structures and ribs (adapted from Mi and Antonia[12]).

due to experimental errors, because $\omega_x/\omega_{x,\mathrm{rms}}$ must be symmetric about zero as a result of the two-dimensional mean flow. $P(\omega_y)$ (Fig. 4b) displays its peak at $\omega_y/\omega_{y,\mathrm{rms}}=0$. The peak in $P(\omega_x)$ and $P(\omega_y)$ at $Re=1.0\times10^4$ drops considerably. This is more evident for $P(\omega_x)$ and $P(\omega_x)$ at $Re=1.0\times10^4$, broadening appreciably for $\omega_x/\omega_{x,\mathrm{rms}}<\pm2$ if compared with $Re=2.5\times10^3$ and 5.0×10^3. The observation is internally consistent with the increasing relatively small-scale fluctuations (Fig. 3) as Re increases. Presumably, the broadening is largely linked to the increased Kelvin–Helmholtz vortices. The more appreciable broadening in $P(\omega_x)$ than in $P(\omega_y)$ suggests that Kelvin–Helmholtz vortices tend to be aligned streamwise, consistent with direct numerical simulation.[29] This further suggests a connection between Kelvin–Helmholtz vortices and the rib structures, which are generally considered to be quasi-longitudinal[26] (Fig. 5).

$P(\omega_z)$ exhibits twin peaks (Fig. 4c). The peak of negative vorticity is due to the spanwise vortices of negative sign that occur at $y/d>0$, whereas that of positive vorticity is attributed to the spanwise vortices of positive sign, whose center is at $y/d<0$. At $x/d=10$, the centers of both positive and negative vortices occur near the centerline (e.g., Zhou et al.[30]). Therefore, the vortices of both signs can be detected at $y/d=0.6$. As Re increases from 2.5×10^3 to 1.0×10^4, $\omega_z/\omega_{z,\mathrm{rms}}$ corresponding to the negative peak approaches zero, moving from -0.47 to -0.20 (mostly between $Re=5.0\times10^3$ and 1.0×10^4). This variation suggests a reduction in the most likely spanwise vorticity magnitude at the vortex center. Accordingly, the time-averaged normalized spanwise vorticity (not shown) decreases in magnitude as Re increases. The three-dimensionality, along with the viscous dissipation, mixing of opposite-signed vorticities, entrainment, and nonlinear effects, may cause a loss of spanwise vorticity.[31] The three-dimensionality results from the slant of spanwise vortex rolls and the occurrence of predominantly longitudinal structures such as Kelvin–Helmholtz vortices. The assertion is corroborated by faster growing rms values, $\omega_{x,\mathrm{rms}}$ and $\omega_{y,\mathrm{rms}}$, relative to $\omega_{z,\mathrm{rms}}$, as discussed in the next subsection.

C. Reynolds Stresses and rms Vorticity

The normalized Reynolds normal stresses across the wake, $\overline{u^{2*}}$, $\overline{v^{2*}}$, and $\overline{w^{2*}}$, are shown in Fig. 6 for $x/d=10$–40. The Reynolds stresses in a circular cylinder wake have been extensively documented in the literature.[12,13,28,30,32–35] The near wake of a circular cylinder is developing and the Reynolds normal stresses increase with Re. As a result, the agreement in $\overline{u^{2*}}$ and $\overline{v^{2*}}$ between the present and previous data is good for comparable Re but not so for different Re. The Re dependence of the Reynolds normal stresses appear less evident for a larger x/d. On the other hand, the Reynolds shear stress exhibits little dependence on Re.

Figure 7 presents the cross-flow distribution of the rms values, $\omega^*_{x,\mathrm{rms}}$, $\omega^*_{y,\mathrm{rms}}$, and $\omega^*_{z,\mathrm{rms}}$, of the three vorticity components. The ratio of rms vorticity values at the centerline and $y/d\approx7$, which may be considered to be approximately in the free stream, is between

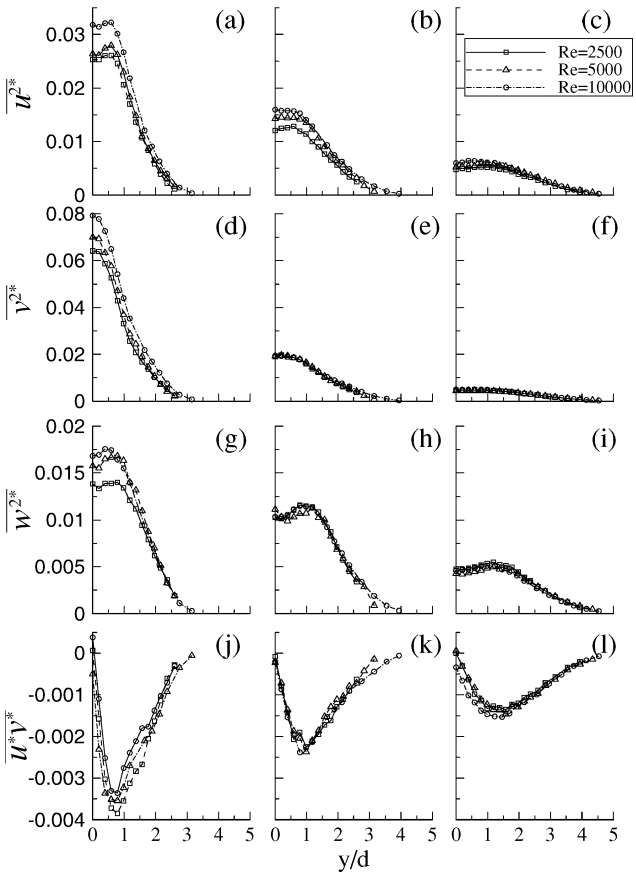

Fig. 6 Time-averaged Reynolds normal stress, Reynolds shear stress, and spanwise vorticity distributions across the wake: a–c) u^{2*}: $x/d=10$, 20, 40; d–f) v^{2*}: 10, 20, 40; g–i) w^{2*}: 10, 20, 40; and j–l) $\overline{u^*v^*}$: 10, 20, 40.

40 and 150 for different Re, indicating a good signal-to-noise ratio. For the purpose of comparison, previous measurements[9,12,13] are also included in the figure. Zhang et al.'s[13] measurement was conducted at $Re=5.6\times10^3$. But, due to poor spatial resolution ($3.5\sim5$ mm), their data are even smaller than the present measurement at $Re=2.5\times10^3$. Mi and Antonia[12] used a four-wire probe (consisting of two X wires separated by a distance of 1.2 mm) and applied a correction to the measured rms values. As a result, their $\omega^*_{y,\mathrm{rms}}$ and $\omega^*_{z,\mathrm{rms}}$ were considerably larger than the present data at $Re=2.5\times10^3$. Marasli et al.[9] procured their measurement at $x/d=30$ using a 12-wire probe with a spatial resolution of about 2 mm. Because vorticity experiences fast streamwise decay, the difference in x/d along with a lower Re ($=2.0\times10^3$) contributes to the

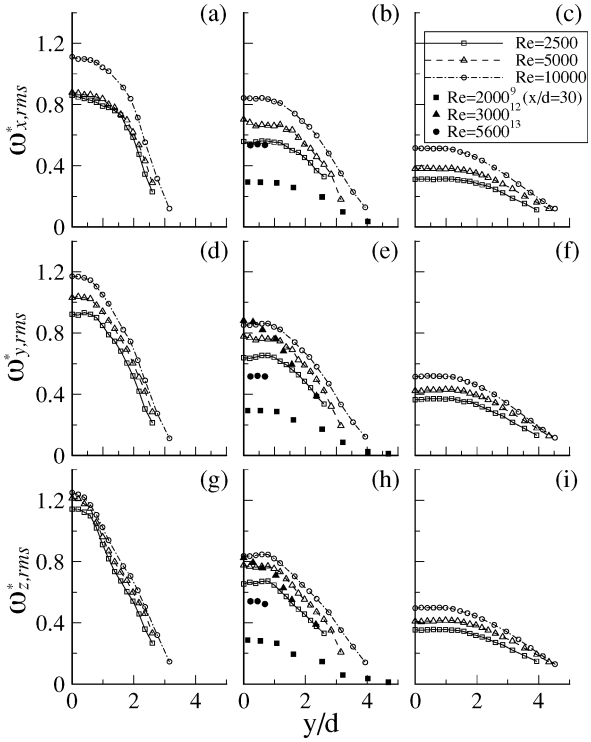

Fig. 7 Lateral distribution of the rms vorticity across the wake: a–c) $\omega^*_{x,\mathrm{rms}}$: $x/d = 10, 20, 40$; d–f) $\omega^*_{y,\mathrm{rms}}$: 10, 20, 40; and g–i) $\omega^*_{z,\mathrm{rms}}$: 10, 20, 40.

observation that their results are smaller than the present ones. This comparison indicates that the present vorticity measurement is reasonable. The values of $\omega^*_{x,\mathrm{rms}}$, $\omega^*_{y,\mathrm{rms}}$, and $\omega^*_{z,\mathrm{rms}}$ rise with increasing Re. In contrast with $\overline{u^{2*}}$, $\overline{v^{2*}}$, and $\overline{w^{2*}}$, the Re dependence of $\omega^*_{x,\mathrm{rms}}$, $\omega^*_{y,\mathrm{rms}}$, and $\omega^*_{z,\mathrm{rms}}$ persists even at $x/d = 40$. At $x/d = 10$ (Figs. 7a, 7d, and 7g), $\omega^*_{x,\mathrm{rms}}$ and $\omega^*_{y,\mathrm{rms}}$ are considerably smaller than $\omega^*_{z,\mathrm{rms}}$ for $Re \le 5.0 \times 10^3$. However, $\omega^*_{x,\mathrm{rms}}$ and $\omega^*_{y,\mathrm{rms}}$ show a faster growth rate than $\omega^*_{z,\mathrm{rms}}$; $\omega^*_{x,\mathrm{rms}}$, $\omega^*_{y,\mathrm{rms}}$, and $\omega^*_{z,\mathrm{rms}}$ increase by 29%, 27%, and 10%, respectively, from $Re = 2.5 \times 10^3$ to 1.0×10^4. As a matter of fact, the rms values of the three vorticity components are approximately the same at $Re = 1.0 \times 10^4$, which is agreeable with Zhang et al.'s report.[13] As illustrated in Fig. 5, small-scale Kelvin–Helmholtz vortices or rib structures are predominantly aligned in the streamwise direction. The fact that most of the increase in $\omega^*_{x,\mathrm{rms}}$ and $\omega^*_{y,\mathrm{rms}}$ occurs from $Re = 5.0 \times 10^3$ to 1.0×10^4 is consistent with the intensified generation of Kelvin–Helmholtz vortices in this Re range.[8]

IV. Coherent Vorticity Field

A. Phase Averaging

The coherent vorticity field may be extracted using a phase-averaging method.[30,32,33] Briefly, the v-signals from the moving vorticity probe and fixed X wire were both digitally bandpass filtered with the center frequency set at f_o, estimated from the frequency at which a pronounced peak occurred in the v-spectrum, using a fourth-order Butterworth filter. The low- and high-pass frequencies were chosen to be the same as f_o, that is, a zero bandpass width was chosen. Such a choice allows a better focus on the organized structures.

The filtered signal v_f is given by the thicker line in Fig. 8. Two phases of particular interest are identified on v_f, viz.,

$$\text{Phase A: } \frac{\mathrm{d}v_f}{\mathrm{d}t} > 0, \qquad v_f = 0 \tag{5}$$

$$\text{Phase B: } \frac{\mathrm{d}v_f}{\mathrm{d}t} < 0, \qquad v_f = 0 \tag{6}$$

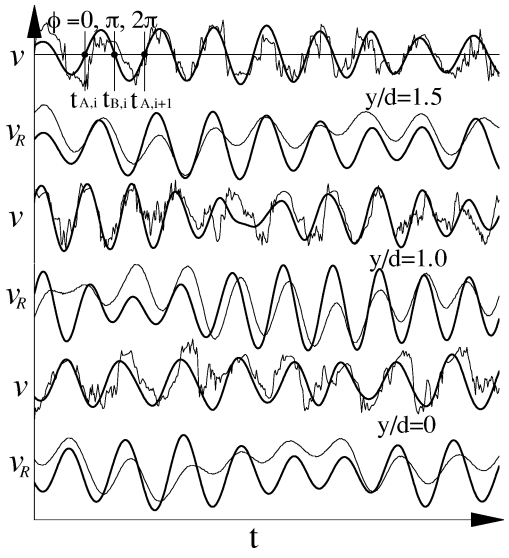

Fig. 8 Signal v from the movable three-dimensional vorticity probe and v_R from the fixed reference probe at $Re = 2.5 \times 10^3$, $x/d = 10$. (The thicker line represents the filtered signal v_f.)

The two phases correspond to times $t_{A,i}$ and $t_{B,i}$ (measured from an arbitrary time origin), respectively. The filtered signal from the vorticity probe was used to determine the phase of the ω_x-, ω_y-, and ω_z-signals from the vorticity probe for averaging, viz.,

$$\phi = \pi \frac{t - t_{A,i}}{t_{B,i} - t_{A,i}}, \qquad t_{A,i} \le t \le t_{B,i} \tag{7}$$

$$\phi = \pi \frac{t - t_{B,i}}{t_{A,i+1} - t_{B,i}} + \pi, \qquad t_{B,i} \le t \le t_{A,i+1} \tag{8}$$

The interval between phases A and B was made equal to $0.5T_o = 0.5/f_o$ by compression or stretching and was further divided into 30 equal intervals. The difference between the local phase at each y-location of the vorticity probe and the reference phase of the fixed X wire probe was used to produce phase-averaged contours of coherent vorticity in the (ϕ, y) plane.

The phase average of an instantaneous quantity B is given by

$$\langle B \rangle_k = \frac{1}{N} \sum_{i=1}^{N} B_{k,i} \tag{9}$$

where k represents phase. For convenience, the subscript k will be omitted. N is about 1800, 2800, and 5200 for $Re = 2.5 \times 10^3$, 5.0×10^3, and 1.0×10^4, respectively.

B. Extract of Coherent Structure

Based on the triple decomposition[36] the variable B can be viewed as the sum of the time mean $\bar{B}$ and the fluctuating component β:

$$B = \bar{B} + \beta \tag{10}$$

where B stands for instantaneous vorticity. The fluctuation β may represent ω_x, ω_y, or ω_z and can be further decomposed into the coherent fluctuation $\tilde{\beta} \equiv \langle \beta \rangle$ and a remainder β_r, viz.,

$$\beta = \tilde{\beta} + \beta_r \tag{11}$$

The coherent fluctuation $\tilde{\beta}(\equiv \langle \beta \rangle)$ reflects the effect from the large-scale coherent structures, while the remainder β_r mainly results from the incoherent structures. Squaring to both sides of Eq. (11) and assuming a negligible correlation between the coherent fluctuation and the remainder yields the equation

$$\langle \beta^2 \rangle = \tilde{\beta}^2 + \langle \beta_r^2 \rangle \tag{12}$$

C. Coherent Vorticity Fields

Figure 9 presents the iso contours of the phase-averaged or coherent vorticity, $\tilde{\omega}_z^*$ at $Re = 2.5 \times 10^3$. The phase ϕ, ranging from -2π to $+2\pi$, can be interpreted in terms of a longitudinal distance, $\phi = 2\pi$ corresponding to the average vortex wavelength. To avoid any distortion of the physical space the same scales are used in the ϕ and y^* directions in Figs. 9 and 10. The positions of centers and saddle points,[28] estimated from sectional streamlines (not shown), are denoted by + and ×, respectively. The $\tilde{\omega}_z^*$ contours (Fig. 9) display the familiar Kármán vortex street (the flow field below $y^* < 0$ is not shown). The vortex center, identified by the maximum concentration of $\tilde{\omega}_z^*$ and marked by +, slowly shifts toward the free stream for increasing x/d, from $y/d \approx 0.3$ at $x/d = 10$ to $y/d \approx 1.0$ at $x/d = 40$. The result agrees with previous reports.[18,21] The maximum concentration of $\tilde{\omega}_z^*$ impairs for a larger x/d. Table 2 lists the maximum magnitude of $\tilde{\omega}_z^*$ at $x/d = 10$, along with previous reports. The present data are in good agreement with Matsumura and Antonia's estimate[33] also obtained using a phase-averaging technique, but are smaller than Hussain and Hayakawa's measurement.[26] The difference may be ascribed to two reasons, different measurement techniques and detection techniques. The present vorticity data should have improved spatial resolution (about 2 mm), compared with Hussain and Hayakawa's data (about 5 mm). Nonetheless, their detections based on vorticity concentrations probably contribute to the higher coherent vorticity concentration. It seems that the maximum $\tilde{\omega}_z^*$ is approximately independent of Re.

Table 2 Maximum magnitude of $\tilde{\omega}_z^*$ at different Reynolds numbers

Re	$\tilde{\omega}_z^*$
2.5×10^3	1.09
5.0×10^3	1.02
5.830×10^3 (Ref. 33)	1.03
1.0×10^4	0.94
1.3×10^4 (Ref. 26)	1.09

The present phase-averaging technique based on spanwise vortices is unable to separate coherent and incoherent ω_x or ω_y, whose signs may be randomly given with respect to the spanwise vortex, resulting in the cancellation of positive and negative vorticity during phase-averaging. Therefore, the contours of phase-averaged vorticity variances $\langle\omega_x^2\rangle^*$, $\langle\omega_y^2\rangle^*$, and $\langle\omega_z^2\rangle^*$ at $x/d = 10$ are calculated. With a sufficiently large number of detections, the averaged $\langle\omega_x^2\rangle^*$, $\langle\omega_y^2\rangle^*$, and $\langle\omega_z^2\rangle^*$ over one wavelength of spanwise vortices should be equal to the corresponding time-averaged vorticity variances, i.e., $\overline{\omega_x^{2*}}$, $\overline{\omega_y^{2*}}$, and $\overline{\omega_z^{2*}}$, respectively, which has been verified (the difference is within 10%). Therefore, the phase-averaged vorticity variances are effectively the sum of the coherent and incoherent structures.

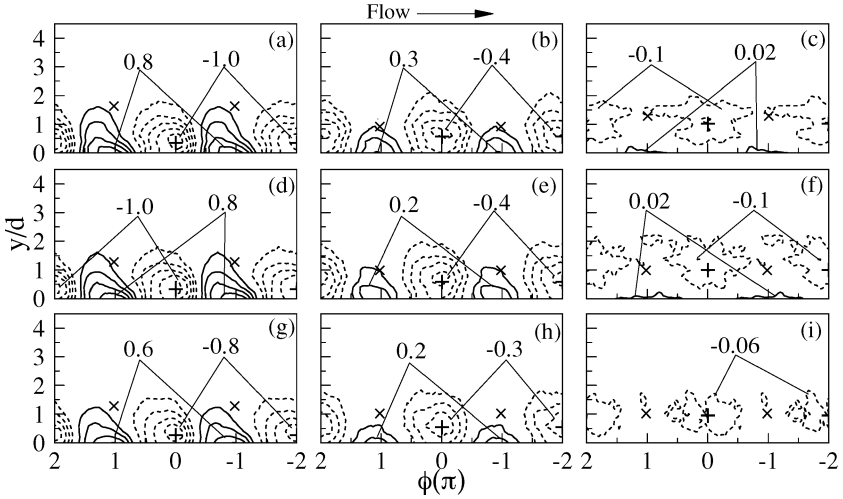

Fig. 9 Phase-averaged vorticity contours $\tilde{\omega}_z^*$: a) $Re = 2.5 \times 10^3$: $x/d = 10$, contour interval = 0.2; b) $Re = 2.5 \times 10^3$: 20, 0.1; c) $Re = 2.5 \times 10^3$: 40, 0.04; d) $Re = 5.0 \times 10^3$: 10, 0.2; e) $Re = 5.0 \times 10^3$: 20, 0.1; f) $Re = 5.0 \times 10^3$: 40, 0.04; g) $Re = 1.0 \times 10^4$; 10, 0.2; h) $Re = 1.0 \times 10^4$: 20, 0.1; and i) $Re = 1.0 \times 10^4$: 40, 0.04. (Centers and saddle points are denoted by + and ×.)

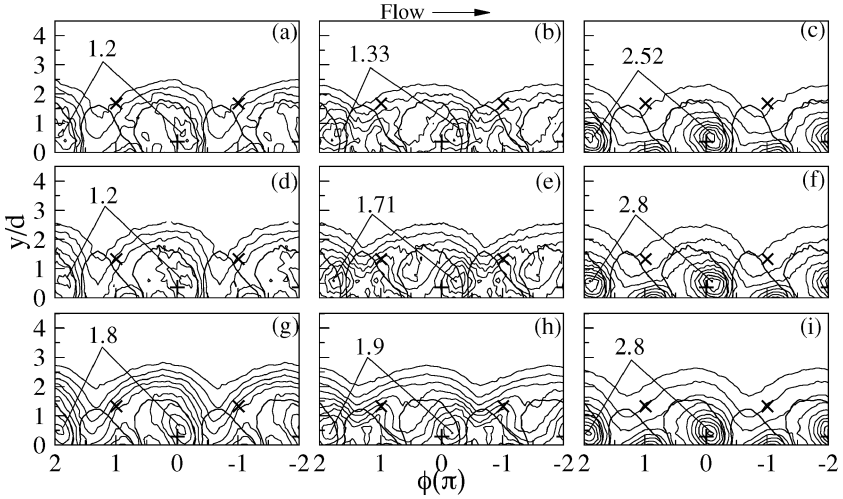

Fig. 10 Contours of phase-averaged vorticity variances at $x/d = 10$: a) $\langle\omega_x^2\rangle^*$: $Re = 2.5 \times 10^3$: contour interval = 0.2; b) $\langle\omega_y^2\rangle^*$: $Re = 2.5 \times 10^3$, 0.19; c) $\langle\omega_z^2\rangle^*$: $Re = 2.5 \times 10^3$, 0.28; d) $\langle\omega_x^2\rangle^*$: $Re = 5.0 \times 10^3$, 0.2; e) $\langle\omega_y^2\rangle^*$: $Re = 5.0 \times 10^3$, 0.19; f) $\langle\omega_z^2\rangle^*$: $Re = 5.0 \times 10^3$, 0.28; g) $\langle\omega_x^2\rangle^*$: $Re = 1.0 \times 10^4$, 0.2; h) $\langle\omega_y^2\rangle^*$: $Re = 1.0 \times 10^4$, 0.19; and i) $\langle\omega_z^2\rangle^*$: $Re = 1.0 \times 10^4$, 0.28. (Centers and saddle points are denoted by + and ×.)

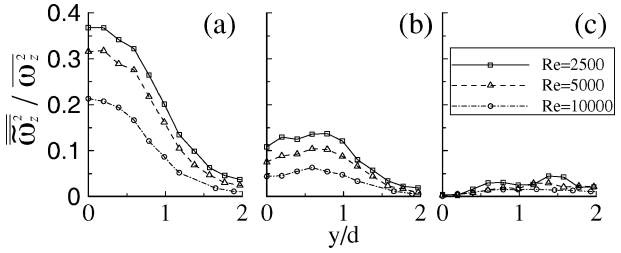

Fig. 11 Coherent contributions to spanwise vorticity variance: $\overline{\overline{\tilde{\omega}_z^2}}/\overline{\omega_z^2}$: $x/d =$ a) 10, b) 20, and c) 40.

The $\langle\omega_z^2\rangle^*$ contours (Fig. 10) display a pattern similar to that of $\tilde{\omega}_z^*$, i.e., the Kármán vortex street, suggesting a predominant contribution from the spanwise structures. [The thicker solid line denotes the outermost vorticity contours of $\tilde{\omega}_z^*$ (Fig. 9.).] Nonetheless, there is an appreciable difference. For example, the maximum $\langle\omega_z^2\rangle^*$ occurs slightly downstream of the vortex center, irrespective of Re. On the other hand, the $\langle\omega_x^2\rangle^*$ and $\langle\omega_y^2\rangle^*$ contours are rather different from those of $\tilde{\omega}_z^*$ for all Re. Their maximum concentrations occur considerably away from the vortex center. The concentrations are probably the combined effect of the three dimensionality of spanwise structures and incoherent structures such as Kelvin–Helmholtz vortices or quasi-longitudinal rib structures. At $Re = 2.5 \times 10^3$, the maximum $\langle\omega_z^2\rangle^*$ is twice as large as those of $\langle\omega_x^2\rangle^*$ and $\langle\omega_y^2\rangle^*$. However, as Re increases, the difference between the maximum $\langle\omega_z^2\rangle^*$ and $\langle\omega_x^2\rangle^*$ or $\langle\omega_y^2\rangle^*$ diminishes. At $Re = 1.0 \times 10^4$, the maximum $\langle\omega_z^2\rangle^*$ is only 55% larger than the maximum $\langle\omega_x^2\rangle^*$ or 47% larger than the maximum $\langle\omega_y^2\rangle^*$. The observation conforms to that of the rms values (Fig. 7) and reconfirms that the three-dimensionality of the flow is enhanced at higher Re.

V. Coherent Contributions to Reynolds Stress and Spanwise Vorticity Variance

Assuming a phase-averaged structure beginning at k_1 samples (corresponding to $\phi = -\pi$) before $\phi = 0$ and ending at k_2 samples (corresponding to $\phi = \pi$) after $\phi = 0$, the structural average, denoted by a double overbar, is defined by

$$\overline{\overline{\tilde{\beta}\tilde{\gamma}}} = \frac{1}{k_1 + k_2 + 1} \sum_{-k1}^{k2} \tilde{\beta}\tilde{\gamma} \tag{13}$$

where β and γ stand for vorticity components. The value of k_1 ($= k_2$) is 30, so that the duration $(k_1 + k_2 + 1)$ corresponds approximately to the average vortex-shedding period. The ratio of $\overline{\overline{\tilde{\beta}\tilde{\gamma}}}$ to $\overline{\beta\gamma}$ provides a measure for the contribution from the coherent structures to the vorticity variance or Reynolds stresses.

As discussed earlier, the coherent component of ω_x or ω_y cannot be extracted at present. Therefore, only the coherent contribution to the spanwise vorticity variance is calculated. Figure 11 shows the cross-flow distribution of $\overline{\overline{\tilde{\omega}_z^2}}/\overline{\omega_z^2}$. Evidently, $\overline{\overline{\tilde{\omega}_z^2}}/\overline{\omega_z^2}$ decreases with an increase in Re; the maximum $\overline{\overline{\tilde{\omega}_z^2}}/\overline{\omega_z^2}$ at $x/d = 10$ (Fig. 11a) is about 37% at $Re = 2.5 \times 10^3$, 32% at $Re = 5.0 \times 10^3$, and 21% at $Re = 1.0 \times 10^4$. The result is consistent with increasing Kelvin–Helmholtz vortices or three-dimensionality of the flow at higher Re. A similar observation is made at $x/d = 20$ and 40 (Figs. 11b and 11c). But the coherent contribution to spanwise vorticity variance reduces rapidly for a larger x/d probably due to the break-up of spanwise structures.

VI. Conclusions

It has been observed that the Reynolds number has a significant influence on the three simultaneously measured components of the vorticity vector. The investigation leads to the following conclusions:

1) The instantaneous vorticity signals exhibit a significantly growing small-scale fluctuations for a higher Re, especially from $Re = 5.0 \times 10^3$ to 1.0×10^4. The Re range coincides with that previously reported of the evident generation of small-scale Kelvin–Helmholtz vortices based on PIV.[8] Correspondingly, the rms values of streamwise and lateral vorticity components increase considerably. The observations indicate a rapidly enhanced three-dimensionality of the flow, which could be ascribed mostly to the effect of Kelvin–Helmholtz vortices.

2) The coherent vorticity field has been calculated based on the measured vorticity. At $Re = 2.5 \times 10^3$, the maximum $\langle\omega_z^2\rangle^*$ is twice as large as that of $\langle\omega_x^2\rangle^*$ or $\langle\omega_y^2\rangle^*$. However, at $Re = 1.0 \times 10^4$, the maximum $\langle\omega_z^2\rangle^*$ is merely 55% larger than the maximum $\langle\omega_x^2\rangle^*$ or 47% larger than the maximum $\langle\omega_y^2\rangle^*$. Correspondingly, the contribution from the coherent structures to spanwise vorticity variance declines considerably. The results suggest increased three-dimensionality of spanwise structures, which is consistent with the perception that the three-dimensionality of the flow is enhanced at higher Re.

3) The maximum spanwise coherent vorticity is approximately independent of Re, at least for the Re range presently investigated.

Acknowledgments

The authors acknowledge support given to them by a Central Research Grant of the Hong Kong Polytechnic University through Grant G-W098. The experiments were conducted at R. A. Antonia's laboratory at the University of Newcastle with financial support from the Australian Research Council.

References

[1]Zdravkovich, M. M., "Conceptual Overview of Laminar and Turbulent Flows past Smooth and Rough Cylinders," *Journal of Wind Engineering Industrial Aerodynamics*, Vol. 33, 1990, pp. 53–62.

[2]Schiller, L., and Linke, W., "Pressure and Friction Drag of Cylinders at Reynolds Numbers 5,000 to 40,000," *Physikalische Zeitschrift*, Vol. 24, 1993, pp. 193–198 (in German).

[3]Roshko, A., and Fiszdon, W., "On the Persistence of Transition in the Near-Wake," *Problems of Hydrodynamics and Continuum Mechanics*, Society for Industrial and Applied Mathematics, Philadelphia, 1969, pp. 606–616.

[4]Gerrard, J. H., "A Disturbance-Sensitive Reynolds Number Range of the Flow past a Circular Cylinder," *Journal of Fluid Mechanics*, Vol. 22, 1965, pp. 187–196.

[5]McCroskey, W. J., "Some Current Research in Unsteady Fluid Dynamics: The 1976 Freeman Scholar Lecture," *Journal of Fluids Engineering*, Vol. 99, 1977, pp. 8–39.

[6]Szepessy, S., and Bearman, P. W., "Aspect Ratio and End Plate Effects on Vortex Shedding from a Circular Cylinder," *Journal of Fluid Mechanics*, Vol. 234, 1992, pp. 191–217.

[7]Unal, M. F., and Rockwell, D., "On Vortex Formation from a Cylinder, Part 1: The Initial Instability," *Journal of Fluid Mechanics*, Vol. 190, 1988, pp. 491–512.

[8]Lin, J. C., Towfighi, J., and Rockwell, D., "Instantaneous Structure of the Near-Wake of a Circular Cylinder: On the Effect of Reynolds Number," *Journal of Fluids and Structures*, Vol. 9, 1995, pp. 409–418.

[9]Marasli, B., Nguyen, P., and Wallace, J. M., "A Calibration Technique for Multi-sensor Hot-Wire Probes and Its Application to Vorticity Measurements in the Wake of a Circular Cylinder," *Experiments in Fluids*, Vol. 15, 1993, pp. 209–218.

[10]Wallace, J. M., and Foss, J. F., "The Measurements of Vorticity in Turbulent Flows," *Annual Review of Fluid Mechanics*, Vol. 27, 1995, pp. 469–514.

[11]Antonia, R. A., Zhou, T., and Zhu, Y., "Three-Component Vorticity Measurements in a Turbulent Grid Flow," *Journal of Fluid Mechanics*, Vol. 374, 1998, pp. 29–57.

[12]Mi, J., and Antonia, R. A., "Vorticity Characteristics of the Turbulent Intermediate Wake," *Experiments in Fluids*, Vol. 20, 1996, pp. 383–394.

[13]Zhang, H. J., Zhou, Y., and Antonia, R. A., "Longitudinal and Spanwise Vortical Structures in Turbulent Near Wake," *Physics of Fluids*, Vol. 12, 2000, pp. 2964–2964.

[14]Wassman, W. W., and Wallace, J. M., "Measurement of Vorticity in Turbulent Shear Flows," *Bulletin of the American Physical Society*, Vol. 24, 1979, p. 1142.

[15]Balint, J-L., Vukoslavcevic, P., and Wallace, J. M., "A Study of the Vortical Structure of the Turbulent Boundary Layer," *Advances in Turbulence*, edited by G. Comte-Bellot and J. Mathieu, Springer, Berlin, 1987, pp. 456–464.

[16]Vukoslavcevic, P., and Wallace, J. M., "Influence of Velocity Gradients on Measurements of Velocity and Streamwise Vorticity with Hot-Wire X-Array Probes," *Review of Scientific Instruments*, Vol. 52, 1981, pp. 869–879.
[17]Tsinober, A., Kit, E., and Dracos, T., "Experimental Investigation of the Field of Velocity Gradients in Turbulent Flows," *Journal of Fluid Mechanics*, Vol. 242, 1992, pp. 169–192.
[18]Zhu, Y., and Antonia, R. A., "Spatial Resolution of a 4-X-Wire Vorticity Probe," *Measurement Science and Technology*, Vol. 7, 1996, pp. 1492–1497.
[19]Perry, A. E., Lim, K. L., and Henbest, S. M., "An Experimental Study of the Turbulence Structure in Smooth and Rough-Wall Boundary Layers," *Journal of Fluid Mechanics*, Vol. 177, 1987, pp. 437–466.
[20]Browne, L. W. B., Antonia, R. A., and Chua, L. P., "Calibration of X Wires for Turbulent Flow Measurements," *Experiments in Fluids*, Vol. 7, 1989, pp. 201–208.
[21]Kawall, J. G., Shokr, M., and Keffer, J. F., "A Digital Technique of the Simultaneous Measurement of Streamwise and Lateral Velocity in Turbulent Flows," *Journal of Fluid Mechanics*, Vol. 133, 1983, pp. 83–112.
[22]Park, S. R., and Wallace, J. M., "The Influence of Instantaneous Velocity Gradients on Turbulence Properties Measured with Multi-Sensor Hot-Wire Probes," *Experiments in Fluids*, Vol. 16, 1993, pp. 17–26.
[23]Tutu, N. K., and Chevray, R., "Cross-Wire Anemometry in High Intensity Turbulence," *Journal of Fluid Mechanics*, Vol. 71, 1975, pp. 785–800.
[24]Zhou, Y., and Antonia, R. A., "Convection Velocity Measurement in a Cylinder Wake," *Experiments in Fluids*, Vol. 13, 1992, pp. 63–70.
[25]Browne, L. W. B., Antonia, R. A., and Chua, L. P., "Calibration of X Wires for Turbulent Flow Measurements," *Experiments in Fluids*, Vol. 7, 1989, pp. 201–208.
[26]Hussain, A. K. M. F., and Hayakawa, M., "Eduction of Large-Scale Organized Structures in a Turbulent Plane Wake," *Journal of Fluid Mechanics*, Vol. 180, 1987, pp. 193–229.
[27]Zhou, Y., and Antonia, R. A., "A Study of Turbulent Vortices in the Near Wake of the Cylinder," *Journal of Fluid Mechanics*, Vol. 253, 1993, pp. 643–661.
[28]Zhou, Y., and Antonia, R. A., "Critical Points in a Turbulent Near-Wake," *Journal of Fluid Mechanics*, Vol. 275, 1994, pp. 59–81.
[29]Williamson, C. H. K., "Vortex Dynamics in the Cylinder Wake," *Annual Review of Fluid Mechanics*, Vol. 28, 1996, pp. 477–539.
[30]Zhou, Y., Zhang, H. J., and Yiu, M. W., "The Turbulent Wake of Two Side-by-Side Circular Cylinders," *Journal of Fluid Mechanics*, Vol. 458, 2002, pp. 303–332.
[31]Zdravkovich, M. M., *Flow around Circular Cylinders, Vol. 1: Fundamentals*, Oxford Univ. Press, Oxford, 1997, pp. 360–361.
[32]Kiya, M., and Matsumura, M., "Turbulent Structure in the Intermediate Wake of a Cylinder," *Bulletin of the Japan Society of Mechanical Engineers*, Vol. 28, 1985, pp. 2617–2624.
[33]Matsumura, M., and Antonia, R. A., "Momentum and Heat Transport in the Turbulent Intermediate Wake of a Circular Cylinder," *Journal of Fluid Mechanics*, Vol. 250, 1993, pp. 651–668.
[34]Kiya, M., and Matsumura, M., "Incoherent Turbulence Structure in the Near Wake of a Normal Plate," *Journal of Fluid Mechanics*, Vol. 190, 1988, pp. 343–356.
[35]Ong. L., and Wallace, J. M., "The Velocity Field of the Turbulent Very Near Wake of a Circular Cylinder," *Experiments in Fluids*, Vol. 20, 1996, pp. 441–453.
[36]Hussain, A. K. M. F., "Coherent Structures—Reality and Myth," *Physics of Fluids*, Vol. 26, 1983, pp. 2861–2850.

W. Dahm
Associate Editor